Three-gap superconductivity in two-dimensional InB_2/InB_4 films

Zhuchi Wang,[1,2] Shuming Zeng,[4] Yinchang Zhao,[3] Xinming Wang,[1,2] and Jun Ni[1,2,*]

[1]*State Key Laboratory of Low-Dimensional Quantum Physics, Department of Physics, Tsinghua University, Beijing 100084, China*

[2]*Frontier Science Center for Quantum Information, Beijing 100084, China*

[3]*Department of Physics, Yantai University, Yantai 264005, China*

[4]*College of Physics Science and Technology, Yangzhou University, Yangzhou 225002, China*

(Received 18 June 2021; revised 12 November 2021; accepted 16 November 2021; published 29 November 2021)

In recent years, multigap superconductors have attracted much attention since the discovery of novel two-gap superconductivity with transition temperature $T_c \sim 39$ K in bulk MgB_2. Based on the first-principles calculation and anisotropic Migdal-Eliashberg theory, we conduct a study on a series of two-dimensional (2D) boron-based materials with doped metal atoms to search for multigap superconductors. We find that InB_2 monolayer films and InB_4 trilayer films are dynamically stable but not synthesized experimentally yet. An evident three-gap superconductor with high $T_c \sim 41.5$ K is obtained in a InB_2 monolayer film. Similarly, InB_4 trilayer film is a novel superconductor with three distinct superconducting gaps and a high $T_c \sim 53$ K. The superconductivity in both 2D films originates mainly from the covalent-state-driven metallization. In addition, the effect of biaxial strain on the superconducting behavior of InB_4 trilayer films is also involved. The InB_4 trilayer films stay dynamically stable under biaxial tensile strain of -3%–6%, and the highest T_c boosts to 64 K under the biaxial tensile strain of $\sim 4\%$. Meanwhile, we also find that the GeB_4 and ZnB_4 trilayer films are two-gap superconductors with high $T_c \sim 48.5$ and 32 K, respectively.

DOI: 10.1103/PhysRevB.104.174519

I. INTRODUCTION

Since the discovery of two-gap superconductivity ($T_c \sim 39$ K) in bulk MgB_2 [1], plenty of studies have been conducted to explore the origin of these gaps and their effects [1–8]. For bulk MgB_2, the electronic states formed by boron orbital planes strongly couple with corresponding phonon modes and B-σ bands contribute strongly to the density of states at Fermi level, which is favorable for electron-phonon-coupling (EPC) formation. This reveals the origin of high T_c and multiple gaps in bulk MgB_2 [4,9]. The Fermi surface (FS) of MgB_2 is formed by bands with completely different electron orbital projections. The in-plane $\sigma(s + p_{x,y})$-bonding state, together with out-of-plane $\pi(p_z)$ lead to the separation of superconducting gaps; the σ gap $\Delta_\sigma \sim 7$ meV is obtained by the former and the weaker π gap $\Delta_\pi \sim 2$–3 meV is obtained by the latter.

The multigap superconductors have many novel physical effects such as anomalous vortical and skyrmionic states [10,11], giant-paramagnetic response [12], hidden criticality [13,14], time-reversal symmetry breaking [8,15], etc. Many efforts are taken to search for robust multigap superconductors (especially beyond two-gap) to confirm these predictions, yet only a few candidates were discovered, such as CaC_6, hole-doped graphane C_2H_2 [16], CaBeSi crystal (which is isostructural and isoelectronic to MgB_2) [17], and two molecular hydrogen structures under extremely high pressure [18]. However, the superconducting gap separation is indistinguishable, and the T_c is extremely low (~ 0.4 K) [17].

Similar to bulk MgB_2, monolayer MgB_2 is a three-gap superconductor with a critical temperature of 20 K through theoretical predictions, which can be increased to 50 K under biaxial strain of $\sim 4\%$ [19]. Compared with the two-gap superconductor bulk MgB_2, the surface states of monolayer MgB_2 are comparable in electronic density to the bulklike σ and π bands. The three-gap superconductivity nature of monolayer MgB_2 originates from the emergent surface contribution [19]. Two AA-stacked honeycomb boron planes with a triangular Mg metal layer as an interlayer can form MgB_4 trilayer film, which is predicted to have a novel four-gap superconductivity with high $T_c \sim 52$ K [20]. The separation between the EPC strength distributions on the σ_1 and σ_2 sheets leads to the evident four-region distribution characteristics, which are responsible for the high-T_c four-gap superconductivity [20]. Atomic doping and substitution are used to search for new superconductors. It is found that defects in the boron sublattice (nonstoichiometric MgB_{2-y}) are not favorable for superconductivity [21]. However, hole doping of MgB_2 or isoelectronic substitution of Mg is a feasible way to find other boron-based superconductors. It is shown that AlB_2 monolayers reveal a two-gap superconducting nature with a high $T_c \sim 26.5$ K. When increasing the number of boron layers (AlB_{2+x}), the surface boron atom layers on both sides enhance the superconductivity; the T_c of B_2-Al-B_2-type AlB_4 boosts to 47 K with robust three-gap superconducting behavior [22].

Although several multigap superconductors such as MgB_4 [20] and AlB_{2+x} [22] have been discovered, many stable structures composed of boron atom layers and other metal atom layers (especially transition metals) have not been reported yet. A novel multigap superconducting nature may exist in

*junni@mail.tsinghua.edu.cn

these structures. In this paper, we conduct a first-principles study and use the fully anisotropic Migdal-Eliashberg theory to investigate the pairing mechanism and multigap superconducting nature in a series of boron-based two-dimensional (2D) materials, in particular, the sandwich-type trilayer films. The most important discovery is that the stoichiometric InB_2 monolayer films and InB_4 trilayer films have three separated superconducting gaps with high $T_c \sim 41.5$ K and $T_c \sim 53$ K, respectively. Moreover, the T_c of InB_4 trilayer films can be increased to $\sim$64 K under biaxial tensile strain of 4%. We also find the two-gap superconductor ZnB_4 with $T_c \sim 32$ K and the two-gap superconductor GeB_4 with high $T_c \sim 48.5$ K.

II. METHODOLOGY

We performed first-principles calculations based on density-functional theory [23,24] with local density approximation. The subsequent lattice vibration properties are based on density-functional perturbation theory calculations [25,26], as coded in the QUANTUM ESPRESSO package [27]. We use plane waves with a kinetic energy cutoff of 80 Ry to simulate the valence electrons, and norm-conserving pseudopotentials to simulate the ion cores. A larger vacuum layer of 18 Å is used to remove the interlayer interaction. The kinetic energy cutoff (Ry) for charge density is set to 220 Ry. All the 2D film structures are fully optimized until the Hellman-Feynman force on each atom is under 10^{-6} Ry/bohr. A $40 \times 40 \times 1$ k-point mesh with a Methfessel-Paxton smearing [28] of 0.02 Ry is set to simulate the Brillouin zone (BZ) integral in the wave-vector space, and a q-point mesh of $10 \times 10 \times 1$ is set in the subsequent lattice dynamics calculations.

The superconducting properties of these films are investigated through the EPW code [29–31]. We solve fully anisotropic Migdal-Eliashberg equations through an imaginary axis at the fermion Matsubara frequencies $\omega_j = (2j + 1)\pi T$ (j is an integer) for a series of temperatures with the same interval. The electronic-phonon interpolation technique applied in the EPW code, which is based on the maximum localized Wannier function, is an efficient and accurate method to calculate the superconducting gaps and T_c. The precedent computations of the electronic wave functions required for the Wannier interpolations are carried out within a uniform unshifted BZ k-mesh of $20 \times 20 \times 1$. An interpolated k-point grid of $300 \times 300 \times 1$ and a q grid of $150 \times 150 \times 1$ are set to solve the anisotropic Migdal-Eliashberg equations. The fermion Matsubara frequencies cutoff is set to be 1.0 eV. The Morel-Anderson pseudopotential μ_c^* is a semiempirical parameter to solve the numerical solution of the Eliashberg equation, defined as $\mu_c^* = \mu^*/[1 + \mu^* \ln(\omega_{el}/\omega_{ph})]$, where ω_{el} and ω_{ph} are the characteristic electron and phonon energy, respectively, and μ^* is the Coulomb potential [7]. A reasonable value is in the range of 0.1–0.2 [7]. In this work, we set $\mu_c^* = 0.13$, the same as that used in the previous materials [19,20,22].

III. RESULTS AND DISCUSSION

In this work, we construct a series of boron-based films through the replacement of the Mg atoms by metals in the fourth and fifth periods of the periodic table in the monolayer MgB_2 films and MgB_4 trilayer films. We first investigate the phonon spectrum of these films to verify the dynamic stability. We find that only the InB_4, ZnB_4, AgB_4, and GeB_4 trilayer films and the InB_2 monolayer films are dynamically stable. So far, these films have not been reported experimentally. We mainly focus on InB_2 and InB_4 to reveal the formation mechanism of the three-gap superconductivity and the regulation of the superconductivity under biaxial strain. In general, the superconductivity of the trilayer films is better than that of the monolayer film [20]. For example, the T_c of theMgB_4 trilayer film is higher than monolayer film MgB_2. Interestingly, The InB_4 trilayer film has a higher $T_c \sim 53$ K than that of monolayer InB_2 ($T_c \sim 42$ K), while monolayer InB_2 shows a three-gap superconducting nature with a slight split in the strongest superconducting gap, which shows more interesting multigap superconductivity.

Figure 1 shows the crystal structures, FSs, corresponding band structures with orbital projections, and the electronic density of states (EDOS) of monolayer InB_2 and trilayer InB_4. As is shown in Fig. 1(a), the monolayer InB_2 film consists of a triangular indium lattice and a honeycomb boron layer. There are four bands crossing the FS; the hexagonal and petal-shaped Fermi sheets surrounding the Γ point are contributed mainly by B-σ electrons (marked as the σ_1 and σ_2 sheets, respectively). This gives rise to two hole pockets surrounding the BZ center and causes a covalent-state-driven metallization, similar to the case in bulk MgB_2 [32–35], boron-doped diamond [36–38], and 2D boron sheets [38–41]. The circle Fermi sheet near the BZ boundary represents the band with B-π states (marked as π sheet); the outermost petal-shaped Fermi sheet at the edge of the BZ boundary represents the band with the hybridized states of the B-π and In-σ orbitals (marked as μ sheet). This is verified by the energy band with orbital projections in Fig. 1(c). The coexistence of σ_1, σ_2, μ, and π sheets indicates that the InB_4 trilayer film may show novel properties of multigap superconductivity. Compared with monolayer InB_2, InB_4 trilayer film has an extra honeycomb boron plane, which has a B_2-In-B_2 sandwich structure. The FS of trilayer InB_4 is similar to that of monolayer InB_2. There are six bands crossing the FS. Due to the existence of two boron planes, B-σ_1 and B-σ_2 sheets form two approximately hexagonal and two petal-shaped Fermi sheets respectively, which forms two pairs of hole pockets near the BZ center.

We proceed to concentrate on the vibrational properties and EPC of the monolayer InB_2 and trilayer InB_4 films. The phonon spectra with the projection of EPC parameters $\lambda_{q\nu}^{\mathrm{ph}}$, together with the phonon density of states (PDOS), and total and mode-resolved corresponding Eliashberg spectral function $\alpha^2F(\omega)$ with the cumulative EPC strength $\lambda(\omega) = 2\int_0^{\omega} \alpha^2F(\omega')/\omega' d\omega'$ are shown in Fig. 2. We can see that the monolayer InB_2 and trilayer InB_4 exhibit similar vibration properties. The absence of imaginary frequency in the phonon spectra indicates that monolayer InB_2 monolayer film is dynamically stable. As for InB_4 trilayer film, there is a slight imaginary ($\sim$0.44 meV) frequency at the Γ point. To further verify whether trilayer InB_4 is dynamically stable, we recalculate the phonon spectrum and superconducting properties of InB_4 using another similar type of pseudopotential. We find that the slight imaginary frequency of InB_4 disappears and

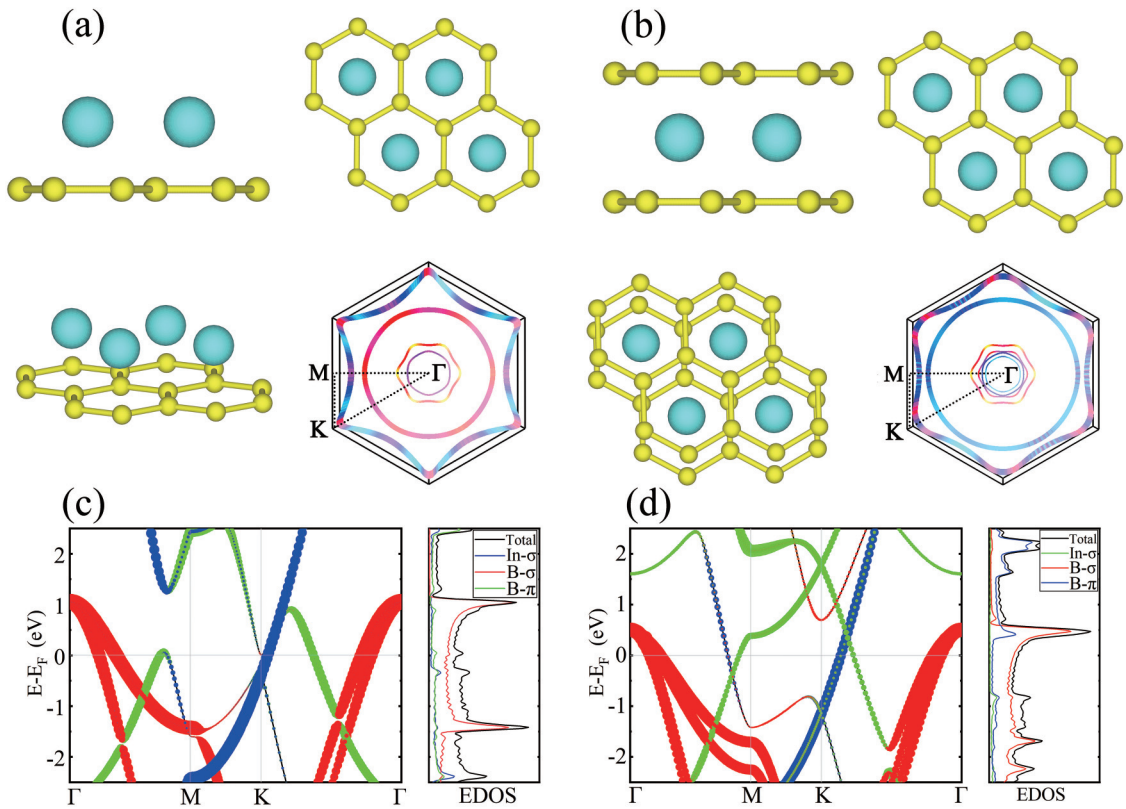

FIG. 1. Crystal structure, Fermi surface (FS), and electronic properties of InB_4 and InB_2. The views of the atomic structure and FSs of (a) monolayer InB_2 and (b) trilayer InB_4. Energy band structures with orbital projections: EDOS of monolayer (c) InB_2 and (d) trilayer InB_4. The red, green, and blue bands represent the Fermi sheets formed by the B-σ states, pure B-π states, and the hybridized states of B-π, and In-σ orbitals, respectively.

shows the same superconducting properties, as is shown in Supplemental Material Fig. S1 in Ref. [42]. This indicates that the InB_4 trilayer film is more likely to be a stable superconductor.

For InB_4 trilayer film, the partial PDOS demonstrates that the phonon modes with frequency under 23 meV are completely dominated by In atoms, while the remaining high frequency modes are mainly dominated by B atoms. Different from monolayer MgB_2 film [19], the stretch of in-plane, out-of-plane B-B atoms of InB_4, which are labeled E_2, B_1 modes (B_{1u}, B_{1g}, two degenerate E_{2u}, and two degenerate E_{2g} modes; see Fig. S2 in Ref. [42]), respectively, cause the optical vibration modes which are softened drastically due to the presence of Kohn anomalies [43] in the Γ point. The region of optical phonon softening in the BZ is highly consistent with the diameter of the hole Fermi sheets caused by the σ-bonding surface boron orbitals, which shows a typical feature of Kohn effect. In addition, the soft mode in InB_4 trilayer films is ∼40 meV, which is comparable with that in other boron-doped diamonds [36,37]. Therefore, the E_2 and B_1 modes near the Γ point dominate the maximum phonon linewidth projection, as shown in Fig. 2(a). In addition, the in-plane modes of the internal B atoms originating from the coupling of B-π orbitals and In-s orbitals also contribute to the projections linewidth, the frequencies of which range from 20 to 60 meV, although the contribution is relatively slight compared with the former.

The mode-resolved $\alpha^2F(\omega)$ and corresponding $\lambda(\omega)$ in Fig. 2(c) further verifies these results. Three low-frequency acoustic phonon branches ($\nu = 1$–3) contribute only 11% of the total EPC coupling strength, while the six high-frequency optical phonon branches ($\nu = 10$–15) contribute 43% and the remaining modes ($\nu = 4$–9) contribute 46%, which is dominant in EPC coupling strength. It is worth noting that contributions of the phonon modes above 23 meV to the EPC strength are consistent with the vibration PDOS distribution. Under the common influence of these phonon modes, the total isotropic EPC parameter $\lambda_{\rm iso}^{\rm ph} = 2\int_0^\infty \alpha^2F(\omega)/\omega\, d\omega$ reaches the value of 0.97 in the InB_4 trilayer film.

The phonon vibration and EPC properties of monolayer InB_2 are almost consistent with that of trilayer InB_4. The B (In) atoms dominate the high- (low-) frequency phonon modes. The E_2 soft modes (two degenerate E_2 modes; see Fig. S3 in Ref. [42]) lead to strong electron-phonon coupling near the Γ point. As shown in Fig. 2(f), the acoustic phonon branches ($\nu = 1$–3) contribute 48% of the total EPC strength, while the high-frequency optical phonon branches ($\nu = 7$–9) and the remaining modes ($\nu = 4$–6) contribute 30% and 22%, respectively, which follows the distribution of PDOS. The calculated EPC parameter $\lambda_{\rm iso}^{\rm ph} = 0.96$ is slightly lower than that of trilayer InB_4.

By solving the fully anisotropic Migdal-Eliashberg equation for self-consistent solution with the Coulomb

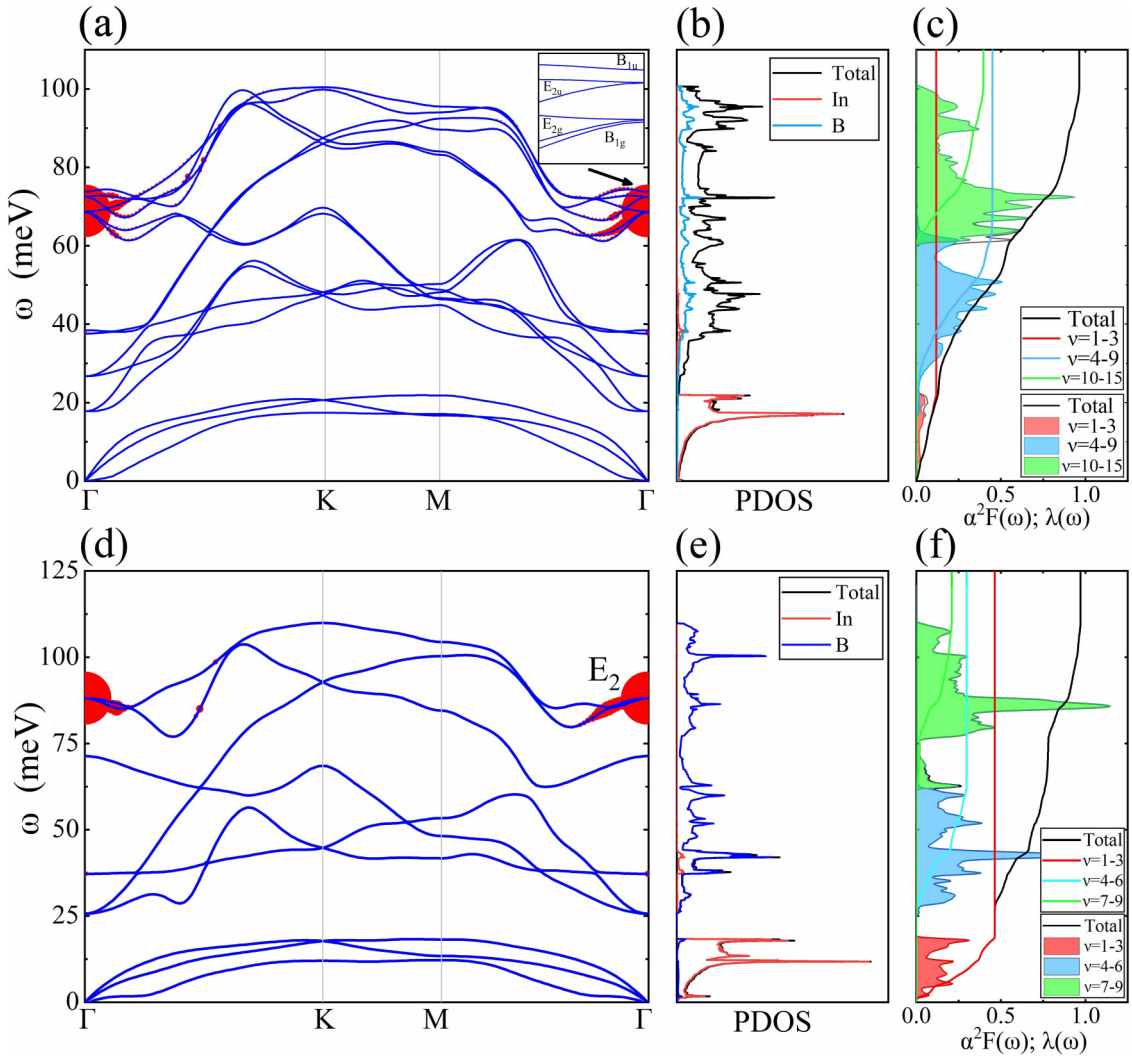

FIG. 2. Lattice dynamics and phonon EPC characteristics of trilayer InB_4 and monolayer InB_2. Phonon spectra with a projection of EPC parameters $\lambda_{qv}^{\mathrm{ph}}$ (red), phonon density of states (PDOS), and total and mode-resolved isotropic Eliashberg function $\alpha^2F(\omega)$ with the corresponding EPC strength $\lambda(\omega)$ of (a)–(c) trilayer InB_4 and (d)–(g) monolayer InB_2.

pseudopotential $\mu_c^* = 0.13$, we can analyze the superconducting gaps based on the normalized superconducting density of states (SDOS), momentum-resolution gaps Δ_{nk} on the FS, and the energy distribution of the gap $\Delta_{nk}(\omega = 0)$ versus temperature T. The normalized SDOS is obtained from the isotropic gap $\Delta(\omega)$ on the real axis via [7,29] $\frac{N_S(\omega)}{N_F} = \mathrm{Re}[\frac{\omega}{\sqrt{\omega^2-\Delta^2(\omega)}}]$; the $N_S(\omega)$ and N_F in the formula represent the electron DOS of the superconducting state and the normal DOS at the Fermi level. The calculated energy distribution of the gap $\Delta_{nk}(\omega = 0)$ versus temperature T, SDOS($T = 5$ K), electronic EPC parameters λ_{nk}^{el}, and momentum-resolved superconducting gaps $\Delta_{nk}(\omega = 0)$ on the FS are shown in Fig. 3.

For trilayer InB_4, the regions of superconducting gaps on the FS are consistent with the distributions of electronic EPC parameters λ_{nk}^{el}, as shown in Figs. 3(e) and 3(f), which is associated with the InB_4 band structure in Fig. 1(a). The hexagonal and petal-shape B-σ Fermi sheets lead to the strongest superconducting gap (called σ gap Δ_σ). The outermost hybridized-state-caused petal-shaped Fermi sheets cause the secondary superconducting gap (called μ gap Δ_μ). The circle Fermi sheet gives rise to the the weakest gap (called π gap Δ_π). At the low temperature of 5 K, the three gaps Δ_σ, Δ_μ, and Δ_π have values in the ranges of 9.31–10.73, 4.40–5.58, and 3.24–3.52 meV with the corresponding average values of 10.02, 4.99, and 3.38 meV, respectively. The SDOS ($T = 5$ K) are shown in Fig. 3(c), There are three distinct peaks related to different gaps on the FS, which are labeled Δ_σ, Δ_μ, and Δ_π. As the temperature rises, each energy gap gradually decreases to zero, which follows BCS theory. A high $T_c \sim 53$ K in trilayer InB_4 is obtained. The T_c is the highest among boron-based 2D materials ever discovered; much higher than that of monolayer MgB_2 ($T_c \sim 20$ K) and trilayer AlB_4 ($T_c \sim 47$ K).

All the electronic EPC parameters λ_{nk}^{el} range from $\lambda_{nk}^{el} = 0.48$ to $\lambda_{nk}^{el} = 1.64$. Obviously, the normalized distribution $\rho(\lambda_{nk}^{el})$ of λ_{nk}^{el} verifies the anisotropy of the EPC parameters. The B-σ Fermi sheets have the largest EPC parameters λ_{nk}^{el} and strength distributions $\rho_{nk}^{el,\sigma} \in [1.26, 1.64]$.

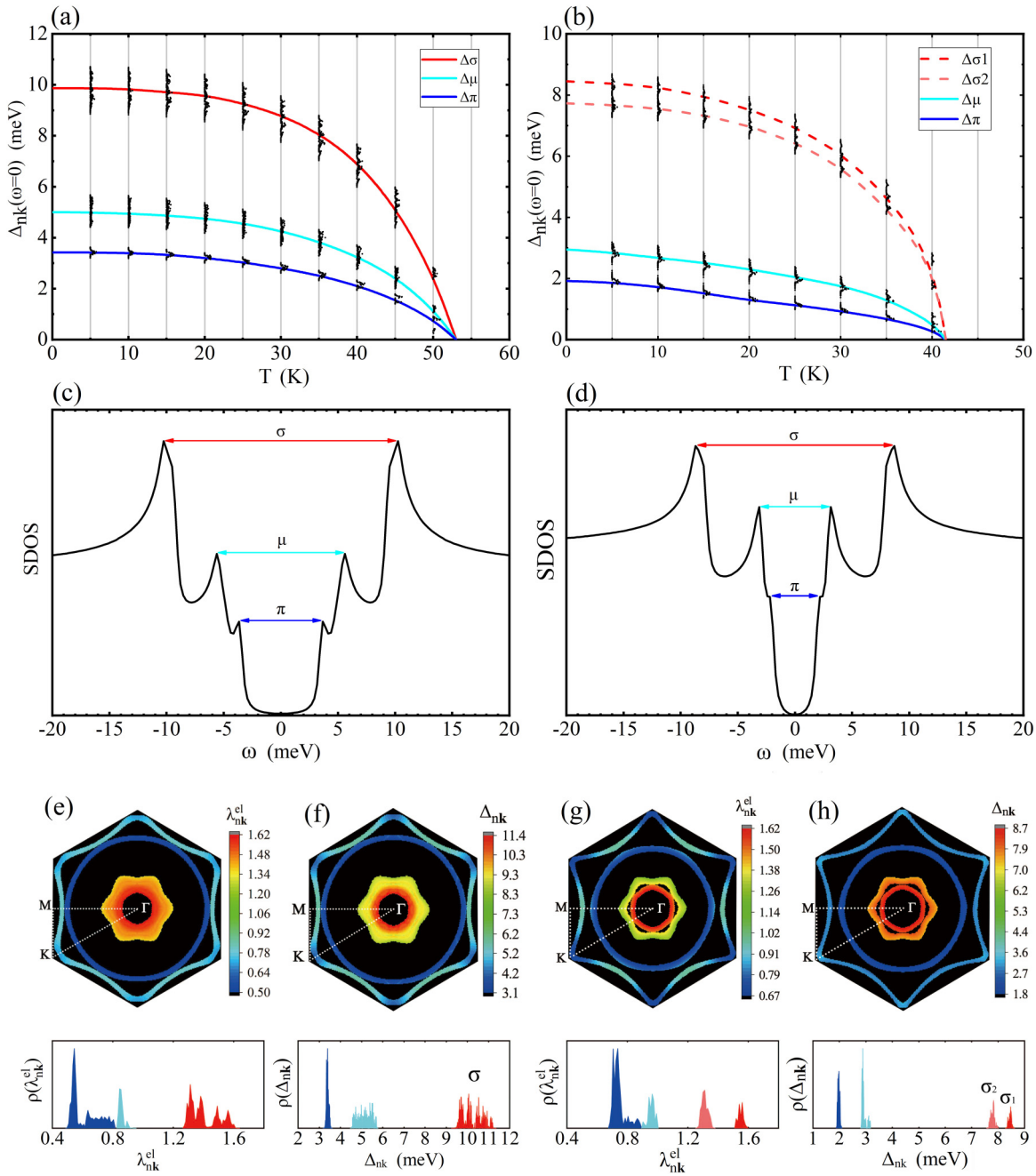

FIG. 3. Energy distribution of the gaps Δ_{nk} versus T for the (a) trilayer InB_4 and (b) monolayer InB_2,. The red, cyan-blue, and blue curves represent the average values of Δ_σ, Δ_μ, and Δ_π, respectively. Superconducting density of states (SDOS) at $T = 5$ K of (c) trilayer InB_4 and (d) monolayer InB_2. The momentum-resolved EPC parameters λ_{nk}^{el} on FS (upper), normalized distribution $\rho(\lambda_{nk}^{el})$ (lower) of (e) monolayer InB_2 and (g) trilayer InB_4. Momentum-resolved superconducting gaps $\Delta_{nk}(\omega = 0)$ on FS (upper), normalized distribution $\rho(\Delta_{nk})$ of energy gaps at 5 K for (f) monolayer InB_2 and (h) trilayer InB_4.

The weaker EPC parameters λ_{nk}^{el} come from μ and π sheets with strength distributions of $\rho(\lambda_{nk}^{el,\mu}) \in [0.83, 0.95]$ and $\rho(\lambda_{nk}^{el,\pi}) \in [0.48, 0.80]$, respectively, which lead to an average electronic EPC parameter of 1.1. It shows that the strongest electronic EPC on the B-σ sheet around the Γ point is created by the optical soft phonons.

We now turn to the multigap superconductivity in monolayer InB_2. The electronic EPC parameters λ_{nk}^{el} on FS and the strength distribution $\rho(\lambda_{nk}^{el})$ of monolayer InB_2 are shown in Fig. 3(g). In general, the distribution of λ_{nk}^{el} on the FS coincides with the regions of Fermi sheets on the FS. Interestingly, the B-σ Fermi sheets form two separated EPC parameters $\lambda_{nk}^{el,\sigma_1}$ and $\lambda_{nk}^{el,\sigma_2}$ with the strength distributions $\rho(\lambda_{nk}^{el,\sigma_1}) \in [1.51, 1.60]$ and $\rho(\lambda_{nk}^{el,\sigma_2}) \in [1.25, 1.38]$, while the weaker EPC parameters λ_{nk}^{el} with the strength distributions $\rho(\lambda_{nk}^{el,\mu}) \in [0.67, 0.89]$ and $\rho(\lambda_{nk}^{el,\pi}) \in [0.89, 1.00]$ are observed on the

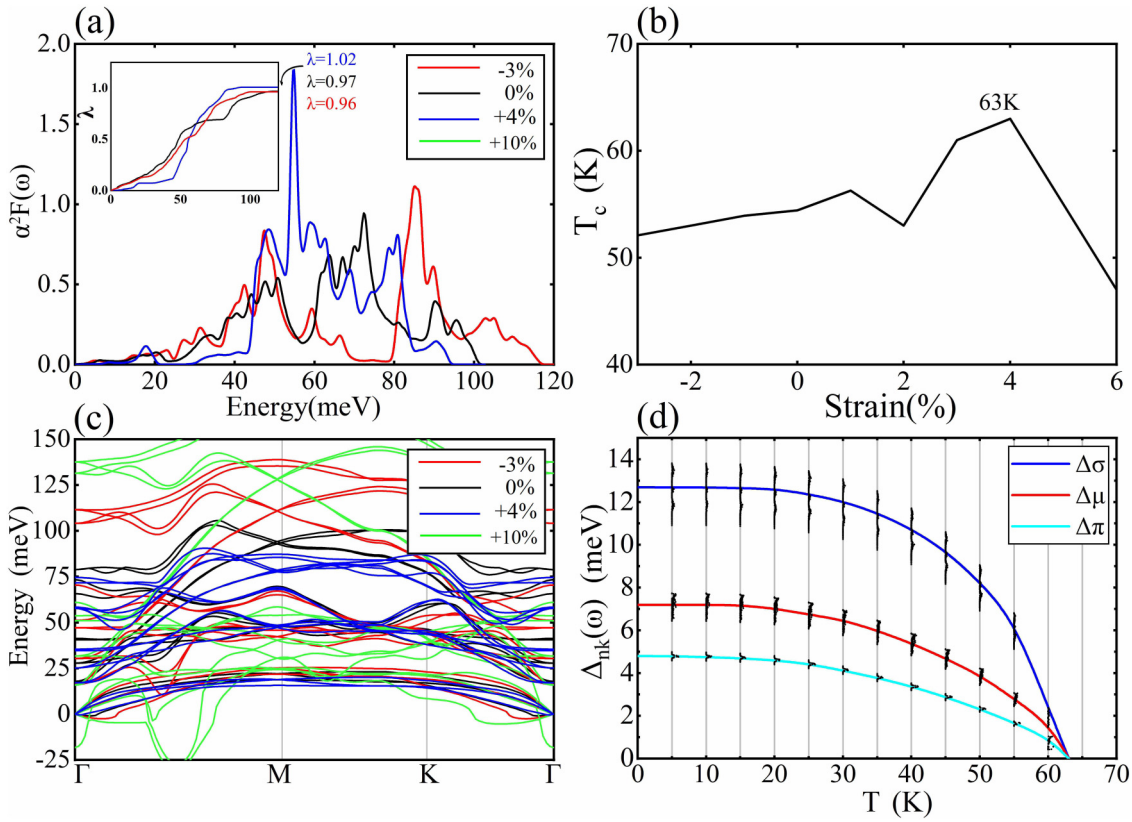

FIG. 4. Phonons spectrum, T_c, EPC parameter λ, Eliashberg function $\alpha^2F(\omega)$, and energy distribution of the gaps of biaxially strained InB_4. (a) The phonon dispersion under the strain of 2%, 4%, 10%, −3%; tensile strain leads to higher phonon frequencies, while compressive strain leads to lower phonon frequencies. (b) T_c versus strain for InB_4 trilayer films. (c) The isotropic Eliashberg function $\alpha^2F(\omega)$ and EPC parameter λ of InB_4 trilayer films under different strains. (d) Energy distribution of the gaps Δ_{nk} versus T for the InB_4 trilayer film under the tensile strain of 4%.

μ and π Fermi sheets. There is no gap between $\lambda_{nk}^{el,\mu}$ and $\lambda_{nk}^{el,\pi}$. However, the $\rho_{nk}^{el,\pi}$ formed by the μ Fermi sheet appears blue at the BZ boundary, which has a distance with the π Fermi sheet. The separation of electronic EPC parameters verifies the anisotropy superconductivity.

As is shown in Fig. 3(h), the energy distribution $\rho(\Delta_{nk})$ has four distinct peaks, which represent four energy gaps on FS. At a low temperature of 5 K, the largest two gaps (called σ_1 gap $\Delta_{\sigma 1}$ and σ_2 gap $\Delta_{\sigma 2}$) formed by the σ_1, σ_2 Fermi sheets have values of 8.31–8.60 and 7.56–8.00 meV, respectively. The weaker gaps (called μ gap Δ_μ and π gap Δ_π) observed on the μ Fermi sheet and the π Fermi sheet have values of 2.81–3.18 and 1.87–2.10 meV, respectively. The average value of Δ_{σ_1}, Δ_{σ_2}, Δ_μ, and Δ_π are 8.46, 7.78, 3.00, and 1.99 meV, respectively. Obviously, Δ_π and Δ_μ, and Δ_μ and Δ_σ are distinctly separated with the separation gap of 0.71 and 4.38 meV, respectively. However, the separation gap between Δ_{σ_1} and Δ_{σ_2} is only 0.31 meV, which is too small to define Δ_{σ_1} and Δ_{σ_2} as two superconducting gaps. The SDOS ($T = 5$ K) only demonstrates three distinct peaks which represent Δ_σ, Δ_μ, and Δ_π. Therefore, monolayer InB_2 is a three-gap superconductor with a slight separation in σ gap Δ_σ. As is shown in Fig. 3(b), we use red ($\Delta_{\sigma 1}$) and pink ($\Delta_{\sigma 2}$) dotted lines to describe the slight separation of the σ gap. The trend of superconducting gaps versus temperature is consistent with the temperature dependence of BCS theory. The gaps Δ_{nk} reveal a four-gap-like superconducting nature at temperatures below 15 K. The Δ_{σ_1} and Δ_{σ_2} gradually become indistinguishable at temperatures above 15 K. The gaps finally vanish at $T_c \sim 41.5$ K.

Besides this, we also calculate the superconductivity in monolayer InB_2 and trilayer InB_4 through the Allen-Dynes formula with $\mu_c^* = 0.13$. A $T_c \sim 13.2$ K is obtained in monolayer InB_2, which is only 31.8% of the value analyzed from multiband theory. For trilayer InB_4, the Allen-Dynes T_c is 28.3 K; much lower than the value ($T_c \sim 53$ K) at temperatures for which the gaps vanish. The T_c's obtained through these two methods demonstrate a huge divergence. Bulk MgB_2 is found to be a two-gap superconductor with high $T_c \sim 39$ K in experiment and the superconducting gaps of bulk MgB_2 vanished at 39.7 K under multigap theoretical calculations [1,9]. This indicates that the multigap theory can predict a higher and more accurate T_c than the Allen-Dynes formula as compared with experiment.

Due to the lattice mismatch in two-dimensional materials, the effect of biaxial strain is considered on the novel three-gap superconductivity in the InB_4 trilayer film. We focus on the biaxial strain applied relative to the in-plane cell parameters, which is the In-In distance with a balance value of $a = 3.04$ Å.

In Fig. 4(a), we compare the equilibrium phonon band structure with the unidirectional strain. The interatomic charge density is depleted as the distance between atoms increases under tensile strain. As a result, the interatomic bonds of structure become hard, leading to the decrease of phonon frequency. However, under compressive strain, the situation is exactly opposite. As is shown in Fig. 4(c), the shift of the $\alpha^2F(\omega)$ peak to lower energy (in line with the general trend of the phonons) and amplification of the $\alpha^2F(\omega)$ peak due to tensile strain cause a great enhancement to the EPC. In general, the tensile strain over the InB_4 trilayer film reduces the overall frequency of the phonon modes, thereby enhancing the EPC strength. Since $\lambda = 2\int_0^\infty d\omega\, \omega^{-1}\alpha^2F(\omega)$ [44], the peaks in lower frequency have a larger contribution to λ. Electron-doped and hole-doped graphenes show a similar trend in the EPC under the influence of biaxial strain in the previous work [45–47]. We further conduct first-principles calculations on the InB_4 trilayer film under strain. The FS is almost consistent with the equilibrium case, which causes the retention of the characteristics of three-gap superconductivity in the InB_4 trilayer film. As shown in Fig. 4(d), for the tensile strain of +4%, the average gaps are $\Delta_\sigma = 12.7$ meV, $\Delta_\mu = 7.3$ meV, and $\Delta_\pi = 4.8$ meV, which are much larger than the equilibrium case, the corresponding EPC parameter $\lambda = 1.02$, leading to the highest critical temperature T_c of 64 K. In the compression case, the critical temperature T_c decreases, but in a much less pronounced way. When the tensile strain exceeds 6% or the compressive stress exceeds 3%, the trilayer InB_4 phonon spectrum shows a large imaginary frequency, and the system becomes dynamically unstable.

In addition, we also find that the GeB_4 and ZnB_4 trilayer films have attractive superconductivity. The momentum-resolved superconducting gaps Δ_{nk} versus T and the SDOS at $T = 5$ K for trilayers GeB_4 and ZnB_4 are shown in Fig. 5. Obviously, the GeB_4 trilayer film is predicted to be a two-gap superconductor with high $T_c \sim 48.5$ K. The σ gap (Δ_σ) and π gap (Δ_π) formed by the σ and π Fermi sheets have values in the ranges of 9.97–11.2 and 5.5–7.5 meV, respectively. As shown in Figs. 5(d)–5(f), the energy gap distributions and two distinct peaks of the SDOS indicate that the trilayer ZnB_4 is also a two-gap superconductor with $T_c \sim 28$ K. The σ gap (Δ_σ) and π gap (Δ_π) originating from the σ and π Fermi sheets have values of 3.51–5.19 and 2.15–2.38 meV, respectively. The calculated Allen-Dynes T_c of trilayer GeB_4 and ZnB_4 is 27.0 and 16.0 K, respectively; much lower than that obtained from multigap theory, which further demonstrates the great influence of the multigap nature in capturing higher T_c.

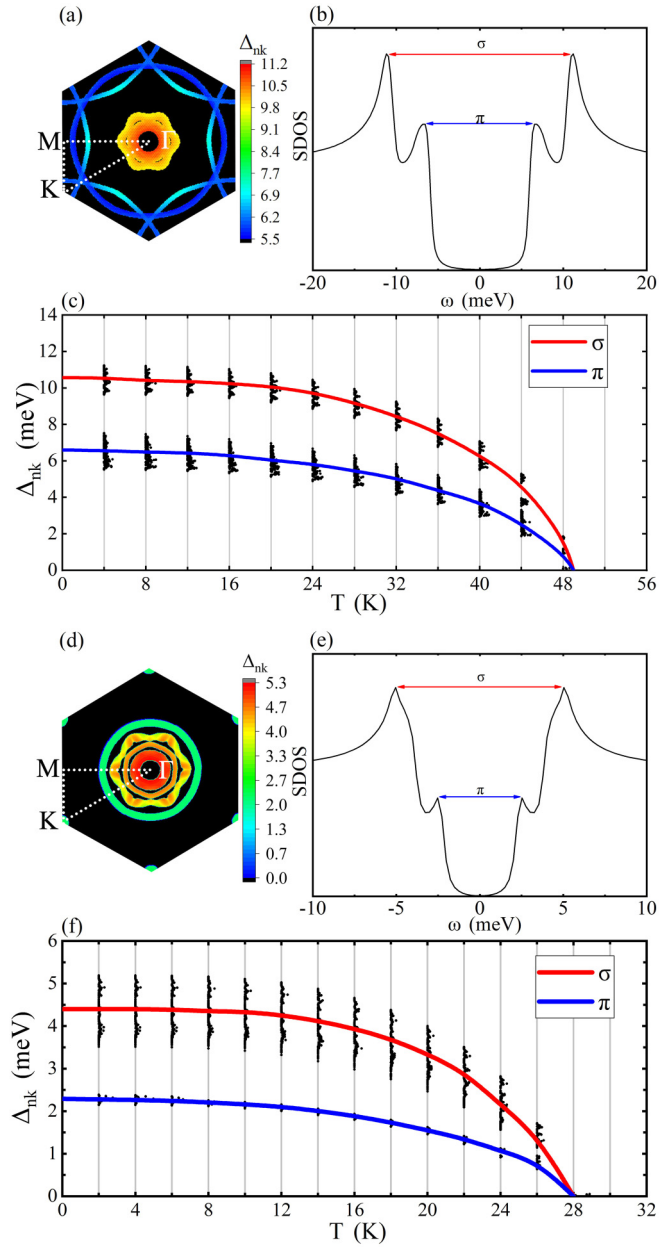

FIG. 5. Momentum-resolved superconducting gaps $\Delta_{nk}(\omega = 0)$ of (a) trilayer GeB_4 and (d) ZnB_4 on FS. Superconducting density of states (SDOS) at $T = 5$ K of (b) trilayer GeB_4 and (e) ZnB_4. Energy distribution of the gaps Δ_{nk} versus T for the (c) trilayer GeB_4 and (f) ZnB_4; the red and blue curves represent the average values of Δ_σ and Δ_π, respectively.

IV. CONCLUSION

In conclusion, we use the fully anisotropic Migdal-Eliashberg theory to investigate the superconductivity in a series of boron-based 2D materials. We find that only the monolayer InB_2, trilayer InB_4, ZnB_4, GeB_4, and AgB_4 are dynamically stable. The InB_4 trilayer film shows a novel three-gap superconducting behavior with high $T_c \sim 53$ K, which originates from the evident three-region distributed strong EPC parameters λ_{nk}^{el}. Three energy gaps Δ_σ, Δ_μ, and Δ_π have average values of 10.02, 4.99, and 3.38 meV. We reveal that the metallization of covalent states in the boron layer and the in-plane phonon modes of surface boron are responsible for the superconductivity. In addition, the T_c can be boosted to 64 K under the tensile strain of 5%. Similarly, the InB_2 monolayer film is a three-gap superconductor with a slight separation in σ gap Δ_σ. Compared with InB_4, the Δ_σ slightly splits as $\Delta_{\sigma 1}$ and Δ_{σ_2} with an energy gap of 0.31 meV; the corresponding electronic EPC parameter λ_{nk}^{el} in the σ_1 and σ_2 Fermi sheets shows distinct separation,

indicating the novel multigap superconducting nature. In addition, we also discover that the trilayer GeB_4 and ZnB_4 are two-gap superconductors with $T_c \sim 48.5$ and 28 K. These findings will promote the search of multigap superconductors.

ACKNOWLEDGMENTS

This research was supported by the National Natural Science Foundation of China under Grant No. 11774195 and Tsinghua University Initiative Scientific Research Program.

[1] J. Nagamatsu, N. Nakagawa, T. Muranaka, Y. Zenitani, and J. Akimitsu, Nature (London) **410**, 63 (2001).

[2] J. Kortus, I. I. Mazin, K. D. Belashchenko, V. P. Antropov, and L. L. Boyer, Phys. Rev. Lett. **86**, 4656 (2001).

[3] T. E. Weller, M. Ellerby, S. S. Saxena, R. P. Smith, and N. T. Skipper, Nat. Phys. **1**, 39 (2005).

[4] M. Iavarone, G. Karapetrov, A. Koshelev, W. Kwok, D. Hinks, G. Crabtree, W. Kang, E.-M. Choi, H. J. Kim, and S.-I. Lee, Superconduct. Sci. Technol. **16**, 156 (2002).

[5] A. Aperis, P. Maldonado, and P. M. Oppeneer, Phys. Rev. B **92**, 054516 (2015).

[6] D. Mou, R. Jiang, V. Taufour, S. L. Bud'ko, P. C. Canfield, and A. Kaminski, Phys. Rev. B **91**, 214519 (2015).

[7] E. R. Margine and F. Giustino, Phys. Rev. B **87**, 024505 (2013).

[8] V. Stanev and Z. Tešanović, Phys. Rev. B **81**, 134522 (2010).

[9] H. J. Choi, D. Roundy, H. Sun, M. L. Cohen, and S. G. Louie, Nature (London) **418**, 758 (2002).

[10] J. Garaud, J. Carlström, and E. Babaev, Phys. Rev. Lett. **107**, 197001 (2011).

[11] E. Babaev, Phys. Rev. Lett. **89**, 067001 (2002).

[12] R. Da Silva, M. Milošević, A. Shanenko, F. Peeters, and J. A. Aguiar, Sci. Rep. **5**, 15569 (2015).

[13] L. Komendová, Y. Chen, A. A. Shanenko, M. V. Milošević, and F. M. Peeters, Phys. Rev. Lett. **108**, 207002 (2012).

[14] M. Silaev and E. Babaev, Phys. Rev. B **85**, 134514 (2012).

[15] N. V. Orlova, A. A. Shanenko, M. V. Milošević, F. M. Peeters, A. V. Vagov, and V. M. Axt, Phys. Rev. B **87**, 134510 (2013).

[16] A. Linscheid, A. Sanna, A. Floris, and E. K. U. Gross, Phys. Rev. Lett. **115**, 097002 (2015).

[17] C. Bersier, A. Floris, A. Sanna, G. Profeta, A. Continenza, E. K. U. Gross, and S. Massidda, Phys. Rev. B **79**, 104503 (2009).

[18] P. Cudazzo, G. Profeta, A. Sanna, A. Floris, A. Continenza, S. Massidda, and E. K. U. Gross, Phys. Rev. Lett. **100**, 257001 (2008).

[19] J. Bekaert, A. Aperis, B. Partoens, P. M. Oppeneer, and M. V. Milošević, Phys. Rev. B **96**, 094510 (2017).

[20] Y. Zhao, C. Lian, S. Zeng, Z. Dai, S. Meng, and J. Ni, Phys. Rev. B **101**, 104507 (2020).

[21] N. I. Medvedeva, A. L. Ivanovskii, J. E. Medvedeva, and A. J. Freeman, Phys. Rev. B **64**, 020502(R) (2001).

[22] Y. Zhao, C. Lian, S. Zeng, Z. Dai, S. Meng, and J. Ni, Phys. Rev. B **100**, 094516 (2019).

[23] D. M. Ceperley and B. J. Alder, Phys. Rev. Lett. **45**, 566 (1980).

[24] J. P. Perdew and Y. Wang, Phys. Rev. B **45**, 13244 (1992).

[25] X. Gonze and B. Amadon, Comput. Phys. Commun. **180**, 2582 (2009).

[26] S. Y. Savrasov and D. Y. Savrasov, Phys. Rev. B **54**, 16487 (1996).

[27] P. Giannozzi, S. Baroni, N. Bonini, M. Calandra, R. Car, C. Cavazzoni, D. Ceresoli, G. L. Chiarotti, M. Cococcioni, I. Dabo *et al.*, J. Phys.: Condens. Matter **21**, 395502 (2009).

[28] M. Methfessel and A. T. Paxton, Phys. Rev. B **40**, 3616 (1989).

[29] S. Poncé, E. Margine, C. Verdi, and F. Giustino, Comput. Phys. Commun. **209**, 116 (2016).

[30] F. Giustino, M. L. Cohen, and S. G. Louie, Phys. Rev. B **76**, 165108 (2007).

[31] F. Giustino, Rev. Mod. Phys. **89**, 015003 (2017).

[32] J. M. An and W. E. Pickett, Phys. Rev. Lett. **86**, 4366 (2001).

[33] A. Y. Liu, I. I. Mazin, and J. Kortus, Phys. Rev. Lett. **87**, 087005 (2001).

[34] K.-P. Bohnen, R. Heid, and B. Renker, Phys. Rev. Lett. **86**, 5771 (2001).

[35] T. Yildirim, O. Gülseren, J. W. Lynn, C. M. Brown, T. J. Udovic, Q. Huang, N. Rogado, K. A. Regan, M. A. Hayward, J. S. Slusky, T. He, M. K. Haas, P. Khalifah, K. Inumaru, and R. J. Cava, Phys. Rev. Lett. **87**, 037001 (2001).

[36] L. Boeri, J. Kortus, and O. K. Andersen, Phys. Rev. Lett. **93**, 237002 (2004).

[37] K.-W. Lee and W. E. Pickett, Phys. Rev. Lett. **93**, 237003 (2004).

[38] Y. Zhao, S. Zeng, and J. Ni, Phys. Rev. B **93**, 014502 (2016).

[39] E. S. Penev, A. Kutana, and B. I. Yakobson, Nano Lett. **16**, 2522 (2016).

[40] Y. Zhao, S. Zeng, and J. Ni, Appl. Phys. Lett. **108**, 242601 (2016).

[41] Y. Zhao, S. Zeng, C. Lian, Z. Dai, S. Meng, and J. Ni, Phys. Rev. B **98**, 134514 (2018).

[42] See Supplemental Material at http://link.aps.org/supplemental/10.1103/PhysRevB.104.174519 for the vibrational, superconducting properties of InB_4 trilayer films and InB_2 monolayer films.

[43] W. Kohn, Phys. Rev. Lett. **2**, 393 (1959).

[44] R. Fogelholm, Ö. Rapp, and G. Grimvall, Phys. Rev. B **23**, 3845 (1981).

[45] J. Pešić, R. Gajić, K. Hingerl, and M. Belić, Europhys. Lett. **108**, 67005 (2014).

[46] C. Si, Z. Liu, W. Duan, and F. Liu, Phys. Rev. Lett. **111**, 196802 (2013).

[47] C. Si, Z. Sun, and F. Liu, Nanoscale **8**, 3207 (2016).